Journal of Sailing Technology 2025, volume 10, issue 1, pp. 329 – 351.
The Society of Naval Architects and Marine Engineers.

Hydrodynamics of Three Slender Models Resembling Pacific Canoe Hulls

Richard G. J. Flay
Department of Mechanical and Mechatronics Engineering, Faculty of Engineering and Design, University of Auckland, New Zealand.

Geoffrey J. Irwin
Department of Anthropology, University of Auckland, Auckland, New Zealand.

Ignazio Maria Viola
School of Engineering, University of Edinburgh, UK, i.m.viola@ed.ac.uk.

Manuscript received August 18, 2025; revision received October 13, 2025; accepted October 29, 2025.

Abstract. Ancient Pacific multi-hull vessels did not appear to have keels, and so the side-force had to be generated by the hulls. It is here hypothesised that the earliest vessels had rounded hulls and were used mainly for sailing downwind. However, evolution and technical innovation have caused a change in shape from circular to Vee, presumably because such shapes are better able to generate side force to enable the vessels to also sail across and against the wind. To investigate whether sharper Vee sections are better at generating side-force than a rounded hull, towing tank tests were carried out on three slender models at fixed sink and trim. At high yaw angles, such as those sailed by sailing vessels without appendages, the rounded hull showed lower drag than the narrower hulls. However, the narrowest hulls allowed higher lift and side force, resulting in the minimum resistance (aligned with the longitudinal axis of the vessel). These results support the hypothesis that narrower Vee-shaped hulls would generate more side-force and lower resistance when at leeway than a rounded hull, and this might have driven the design evolution of ancient Pacific vessels.

Keywords: ancient Pacific canoes; catamarans; upwind sailing; hull hydrodynamics; hull forms; side force.

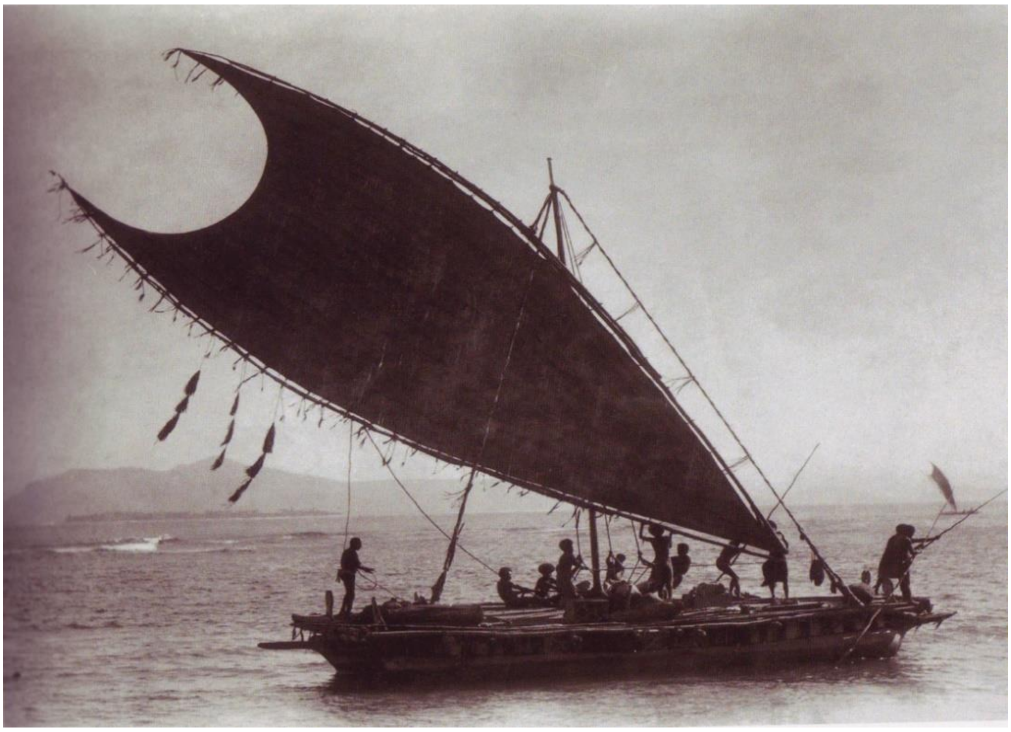

NOMENCLATURE

A	Immersed projected side area [m^2]
C_D	Drag coefficient (based on A) [-]
$\hat{C}_F$	Frictional resistance coefficient (based on S, model scale) [-]
$\hat{C}_{F0}$	Skin friction coefficient (based on S, model scale) [-]
$\hat{C}_{F0fs}$	Full-scale skin friction coefficient (based on S) [-]
C_L	Lift coefficient (based on A) [-]
C_R	Resistance coefficient (based on A) [-]
$\hat{C}_R$	Residual resistance coefficient (based on S) [-]
C_S	Side force coefficient (based on A) [-]
$\hat{C}_T$	Total resistance coefficient (based on S, model scale) [-]
$\hat{C}_{Tfs}$	Full-scale total resistance coefficient (based on S) [-]
$\hat{C}_V$	Viscous resistance coefficient (based on S, model scale) [-]
$\hat{C}_{Vfs}$	Full-scale viscous resistance coefficient (based on S) [-]
$\hat{C}_W$	Wave resistance coefficient (based on S, model scale) [-]
$\hat{C}_{Wfs}$	Full-scale wave resistance coefficient (based on S) [-]
F_D	Drag [N]
F_L	Lift [N]
Fr	Froude number (model scale) [-]
Fr_{fs}	Full-scale Froude number [-]
g	Gravitational acceleration [m s^{-2}]
k	Coefficient of the form factor, $1+k$ [-]
L_{oa}	Length overall [m]
p	Pressure [Pa]
Re	Reynolds number (model scale) [-]
Re_c	Critical Reynolds number [-]
Re_{fs}	Full-scale Reynolds number [-]
S	Wetted surface area, with the model upright and immersed to its waterline [m^2]
t	Water temperature [^{o}C]
V	Test speed [m s^{-1}]
x_{tr}	Laminar-to-turbulent transition coordinate from the bow [m]
λ	Leeway (or yaw) angle [deg.]
ρ	Fluid density [kg m^{-3}]
CFD	Computational Fluid Dynamics
ITTC	International Towing Tank Conference
U	Rounded hull
V1	Wide Vee hull
V2	Narrow Vee hull

1. INTRODUCTION

Understanding the effect of different hull shapes on the hydrodynamic performances of sailing vessels has been essential knowledge for the pioneering colonisation of the oceans. Yet, what were the main drivers for hull shape evolution over the centuries is still poorly understood. East Polynesian canoes, for example, were long and narrow because they were made from dugout logs and sewn planks, and they had a two-spar rig and sail stepped forward (Haddon and Hornell 1997). However, their ability to sail upwind was affected by the underwater cross-sectional hull profile. U-shaped hulls represent the basic shape of a hollowed-out tree trunk and are presumed to be an ancient shape, and they remained common in ethnographic times. In contrast, some of the voyaging canoes recorded during the voyages of James Cook of 1769-1778, were of a wide Vee shape, including

Tahitian *pahi* and Tongan *tongiaki* canoes (Finney 2006). Maritime technology was most developed in Micronesia with sophisticated *proa* outrigger canoes with narrow and deep Vee-shaped planked hulls. The remarkable migrations of the ancient Polynesians were made possible by advances in sailing technology, but what drove the shift from U-shaped to V-shaped hulls is not yet clear.

From west to east the islands became further apart and generally smaller with more contrary winds, and computer simulations of voyaging have found that intentional voyages would be viable when undertaken with vessels capable of sailing efficiently against the wind (Montenegro et al. 2014: 242, Irwin et al. 2022). Therefore, the authors speculate that the earliest vessels with rounded hulls (from trees) were probably used mainly for sailing downwind. However, with time, it would have been realised that sail powered vessels could also manoeuvre across the wind, and then the importance of side force as well as drag would have begun to be appreciated.

The question of the lift or side force developed by U- and V-shaped hulls when at incidence, as well as the drag, are subjects that have been examined by researchers developing velocity prediction programs for modern as well as ancient Pacific vessels, e.g. Jackson (1995), Jackson and Bailey (1996), Jacobs (2003), Flay (2008), and Dudley et al. (2021). Answers to these questions are important for examining the exploration of the Pacific, as discussed in Irwin (1992), Irwin et al. (2024), Irwin and Flay (2015), Irwin et al. (2017), Irwin et al. (2023), and Irwin et al. (2024). The sailing performance of Polynesian craft, and particularly their ability to travel to windward, can help determine under what circumstances (wind speed and direction) a vessel can sail from one island group to another. This question is of much interest to anthropologists, and indeed in recent times voyages have been made in a traditional Kula canoe, Damon (2017). A simulated canoe was sailed in the same recorded weather (Dudley et al., 2021) and the tracks of the courses compared in Irwin et al. (2024). The agreement was good.

The drag of both U- and V-shaped hulls can be determined using the standard approaches of subdividing it into skin friction and residuary resistance. These underwater shapes are similar to those of kayaks for which Jackson (1995) used a simplified drag estimation approach due to Adler (1990). Estimating the drag of such shapes without having to resort to tank testing is relatively straightforward. However, for the lift or side force it is more problematical.

Slender body theory is presented in Thwaites (1987). This theory applies to slender bodies with the onset flow at low incidence and was developed initially to understand the behaviour of airships. It can be applied to the Polynesian canoe hulls by considering only the immersed section, and assuming that the water surface is a plane of symmetry. It was found by Flay (2008) to produce much lower side force than slender wing theory for a Tornado class sailing yacht hull. However, side forces were predicted using slender body theory in Hunter and Joubert (1988) and found to agree rather well with tank test results. However, the shape of their test case was based on a tanker with slab sides and a flat bottom, which is completely unlike the hull shapes that are being considered herein for Pacific canoe hulls.

Katz and Plotkin (2001) describe slender wing theory, which has been used to determine the side force on long slender Oceanic Canoes by Jacobs (2003). A drawback with the basic slender wing theory is that for small aspect ratio wings, the non-linear components of lift are significant (Hoerner and Borst, 1985, van Oossanen, 1981). Also, slender wing theory does not take account of the profile shape, so it will give the same side force for a U- and a V-shaped underwater profile with the same effective aspect ratio, and so this theory does not help in elucidating the differences in the side force developed between U- and V-shaped underwater profiles that are relevant for Polynesian canoe hulls.

This question was of much interest to the Yacht Research Unit and the University of Auckland and so work on this topic was undertaken. A preliminary numerical study by Boeck (2010) and Boeck et al (2012) on three different hulls showed that sharper Vee sections are better at generating side-force than a rounded hull. The three hulls had different displacements but the same draught, which is generally consistent with ethnography and archaeological remains of prehistoric canoes. The displacement of Pacific canoe hulls varied with the method of construction and hulls from dugout logs were generally heavier that those built of planks sewn together. Sensitivity tests have been undertaken to investigate the effect of differences in vessel displacement on the performance of ancient Pacific multi-hull vessels (Irwin et al. 2024). Waterlines were calculated for 18 metre East Polynesian double canoes with medium V-shaped hulls weighing from 6 tons to 24 tons. Displacements below 8 tons are not feasible, and those above 20 tons are not seaworthy. The velocity prediction programme showed that displacement does not have a marked effect on upwind sailing angle, and the same is true for speed. Speeds of canoes of 16-ton displacement remain similar to those of 10 tons, but heavier canoes are slower. It is clear that East Polynesian double canoes with medium V-shaped hulls were well suited to ocean migrations because they could sail upwind with varying loads of people and cargo.

The purpose of the present study is to verify experimentally whether sharper Vee sections are better at generating side-force than a rounded hull, and to analyse the different force components of each hull shape. The paper extends the work presented in Flay et al. (2019). The results of this study provide new insights on ancient vessels, such as the archaeological remains of a range of Māori canoe hull shapes found in wetland sites in New Zealand which date from the period AD 1400-1800 (Johns et al. 2014, Irwin et al. 2017). Furthermore, these results might be of interest for the design of modern multi-hull vessels such as, for instance, the multi hulls developed in the recent past for the America's Cup races.

2. METHODOLOGY

2.1 Newcastle University Towing Tank

Since its construction in 1951 the Towing Tank at Newcastle, Figure 1, has been in almost continuous use. Since then, the tank has been regularly updated to keep abreast of modern trends. This includes the fitting of wave-making and electronic recording equipment. Recent upgrades include the installation of a state-of-the-art motor control system to enhance very slow speed and high-speed testing capabilities. A recent innovation is a modern telemetry system which allows data to be sampled without any wired connections between the carriage and shore-based equipment. Further details are available in Table 1.

The Towing Tank is used mainly for calm water, wave resistance and sea-keeping experiments. Models are towed using a monorail carriage system that has a maximum speed of 3 m/s in its normal mode. The carriage can be remotely or manually controlled, while the 32-channel data retrieval system is on-line to a PC. The wave-makers can be used to generate regular waves of up to 0.12 m in height and wave periods in the range of 0.5 s to 2 s. They are also capable of generating long crested random seas with a variety of wave spectra.

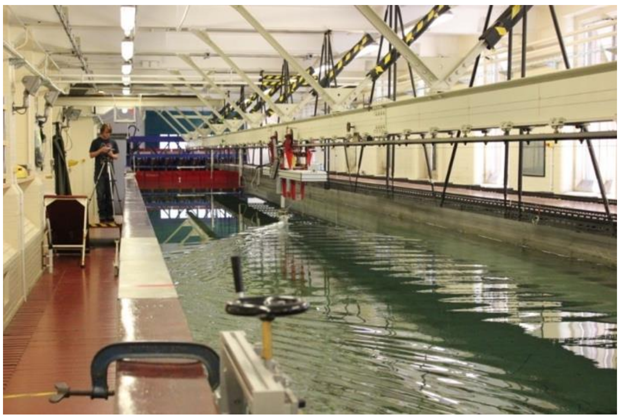

Figure 1. Photograph of the Newcastle University Towing Tank.

Table 1. Towing Tank Specifications.

Specifications	
Tank length	37 m
Width	13.7 m
Water depth	1.25 m
Normal Carriage velocity	3 m/s
Wave capability	
Period range	0.5 s - 2 s
Wave height	0.02 m - 0.12 m (Period Dependent)

2.2 Hull Models

The models were based on those used for the Computational Fluid Dynamics (CFD) investigation by Boeck (2010) and Boeck et al (2012), when Boeck was studying in the Yacht Research Unit at the University of Auckland, and CAD images of the three models can be seen in Figure 2. It was decided to manufacture models for tank testing at the University of Auckland, and since the tank was small, and the models had to be shipped to the UK, a scale of 1:10 was used. The CFD investigation used hulls of length 12 m, and so the models had an overall length (L_{oa}) of 1.2 m. Further details of the models are given in Table 2. They are rather small models, and it was realised once the tests were started that it would have been possible to test larger models at yaw, such as 50% longer, but they would have been more difficult to ship from NZ to the UK and back.

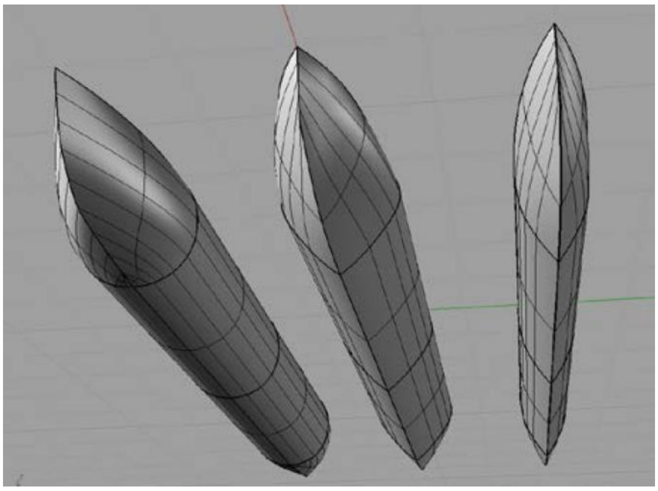

Figure 2. CAD image of the three models used in the CFD investigation from Boeck 2010. Left U – rounded hull, Centre V1 – wide Vee, Right V2 – narrow Vee hull.

Igs files (available in Flay et al. 2022) developed in Boeck 2010 were provided to the Faculty of Engineering Workshop, and these files were used to drive a numerically controlled milling machine to cut the shapes out of blue foam (Styrofoam). The foam models were then covered in a layer of fibre glass and painted, to strengthen them and to make them waterproof. A photograph of the models can be seen in Figure 3. The design waterline is shown in red and is the same for all three models. It was decided that the testing would be based on having constant draft, and hence the displacements of the models varied. The projected side area of all models is the same and is 4.88 m^2 in full-scale, or 0.0488 m^2 in model scale.

Table 2. Model-scale details of the three models used in the CFD and towing tank investigations, Boeck 2010. U – rounded hull, V1 – wide Vee hull, V2 – narrow Vee hull.

	U	V1	V2
Draft amidships [m]	0.046	0.046	0.046
Waterline length [m]	1.16	1.16	1.16
Keel angle [deg]	180	100	70
Displacement [kg]	3.8	2.1	1.3
Wetted surface area [m^2]	0.163	0.129	0.111
Water plane area [m^2]	0.117	0.085	0.054
Projected side area [m^2]	0.0488	0.0488	0.0488
Waterline beam [m]	0.117	0.086	0.054
Prismatic coeff. [-]	0.822	0.823	0.827
Block coeff. [-]	0.492	0.341	0.263
Midship area coeff. [-]	0.753	0.556	0.556
Water plane area coeff. [-]	0.867	0.851	0.856

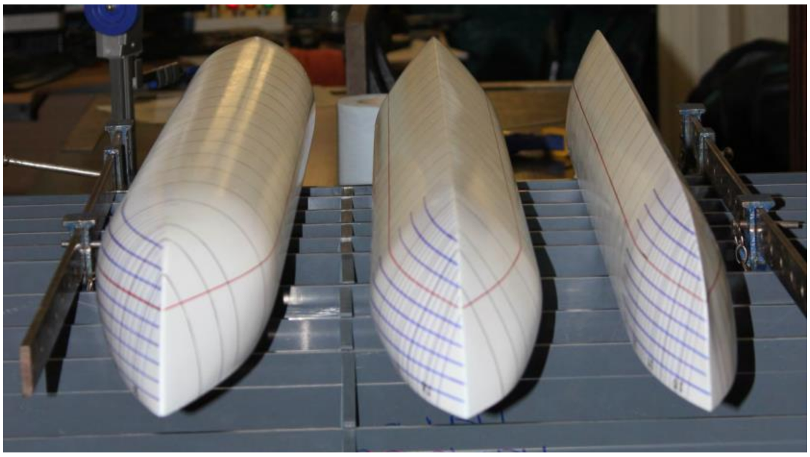

Figure 3. Photograph of the three models showing the underside and the painted grid pattern for assessing wave motion. The water line is shown in red. U (left), V1 (centre) and V2 (right).

2.3 Gifford Dynamometer

A schematic diagram of the Gifford dynamometer is shown in Figure 4. The heave post is attached to the carriage. For fixed sink and trim tests it is clamped so that the model is immersed to the water line when at rest in still water. The pivot base is also secured with rectangular blocks so that it cannot rotate, and during setup the model attitude is adjusted to horizontal using shims. For free to sink and trim tests, the heave post is free to move vertically under the action of the force transmitted to it by the model and the pivot base is free to rotate. The towing plate is rigidly attached to the model, and its angular position is set by screws through holes at predetermined locations. The towing plates can be seen attached to the models in Figure 5. Holes were pre-drilled into the plates at 2° intervals and enabled the larger two models to be tested at leeway angles from 0° up to $\pm$24°. The narrower V2 model could be tested up to $\pm$16°. It was expected that the narrower V2 model would generate more side force for a given leeway angle, which is why it was decided to have a lower maximum leeway angle for this model, although as can be seen in Figure 5, the maximum angle was also limited by the model width.

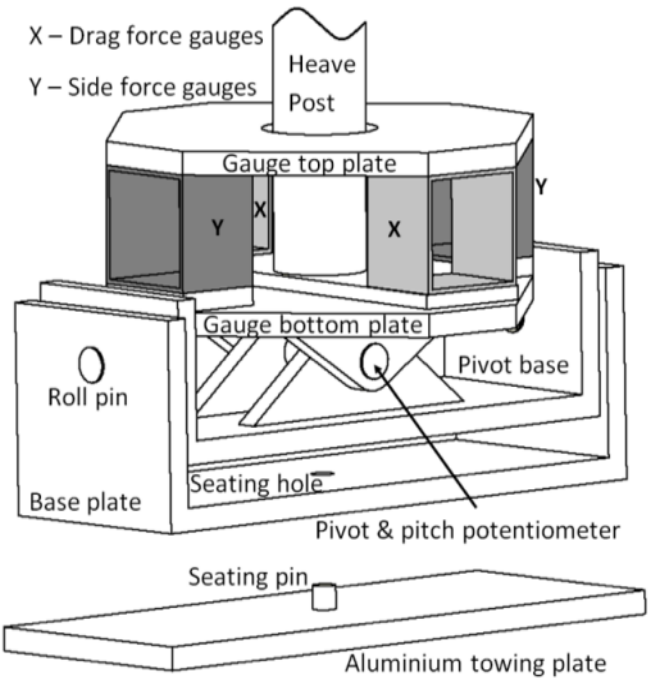

Figure 4. Schematic diagram showing the working principles of the Gifford dynamometer.

2.4 Trip Wire Placement

Trip wires are commonly used on tank test models to fix the location of transition, which would occur further aft at model scale compared to full scale, because of the lower Reynolds number (Re) in the former situation. If we assume that these vessels could travel at say 10 knots or 5 m/s, then based on their overall length of 12 m, the Reynolds number is: $Re_{fs} = 6 \times 10^7$, and the Froude number is: $Fr_{fs} = 0.461$.

If we assume that transition occurs at a critical Reynolds number $Re_c = 5 \times 10^5$, then this would occur at a longitudinal coordinate measured from the bow $x_{tr} = L_{oa}\, Re_c / Re_{fs} = 12\,(5 \times 10^5 / 6 \times 10^7) = 0.1$ m. As a fraction of the length, this is 0.83%. At 5 knots (half the speed) transition would occur at 0.2 m from the bow, which is 1.6% of the length. Thus, in full-scale transition is expected to occur very near the bow. The model scale Reynolds number, Re, is much less. At 10 knots $Fr_{fs} = 0.461$, so for a model scale of 1/10th, the equivalent test speed is given by $V = 1.58$ m/s, and thus $Re = 1.9 \times 10^6$. Assuming as above that transition occurs at $Re_c = 5 \times 10^5$ means that it will occur at 26% of the model length, which is a distance of 0.32 m from the bow. Thus the nature of the flow would be very different, and would be likely to lead to errors in viscous drag.

The approach recommended by the International Towing Tank Conference, ITTC 2002, Rev 01 was taken to determine the location of a trip wire to fix transition. ITTC recommends that a trip wire be located 5% of the length between perpendiculars aft of the forward perpendicular, and that the wire diameter be between 0.5 mm and 1.0 mm. Thus, for all three models, the wires were located a distance 58 mm aft of the FP, which itself is 20 mm aft of the foremost part of the model, so they were 78 mm aft of the foremost part of the model. Note that it is standard practice at Newcastle to use wire of diameter 1.2 mm, and this wire diameter was used on the three models. This slightly larger diameter than that recommended by ITTC could result in a slight increase in drag. An example of the trip wire on model V2 can be seen in Figure 6. The two other models had trip wires at the same location. Thus the trip wire was located a distance 6.5 % of the model length from the bow, i.e. aft of where one might expect transition to occur in full-scale, but well ahead of where it could be expected to occur naturally at model scale.

2.5 Force Coefficients

The main model dimensions are given in Table 2. Coefficients are made dimensionless using the product of area and dynamic pressure. The reference area, A, is normally the immersed projected side area, which is the same for all three models, and so changes in the coefficients relate directly to forces. This decision was made in order to highlight the effect of changes of the hull shape directly on side force and lift, which could have been more difficult to discern if different wetted surface areas had been used for the different hull shapes. However, for some of the analysis, especially for the drag, sometimes the reference area is the wetted surface area, with the model upright and immersed to its waterline. It is given the symbol S. Which reference area is used to form the coefficients is made clear in the relevant text. For example, when applying the Prohaska-Hughes method to relate model to full-scale drag coefficients, it is convenient, and conventional to use the wetted surface area. The density is ρ, and V is the velocity of the model through the still tank water. The ITTC 1999 defines density for g = 9.81 m/s^2 as

$$\rho = 1000.1 + 0.0552\, t - 0.0077\, t^2 + 0.00004\, t^3, \tag{1}$$

where t is temperature of water in °C.

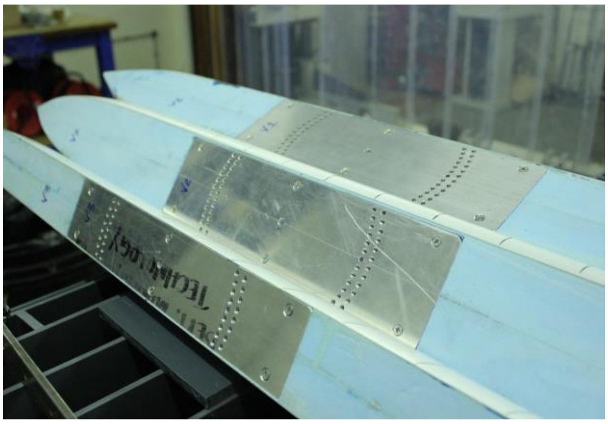

Figure 5. Photograph of models showing attachment of the towing plate with holes pre-drilled at 2° intervals.

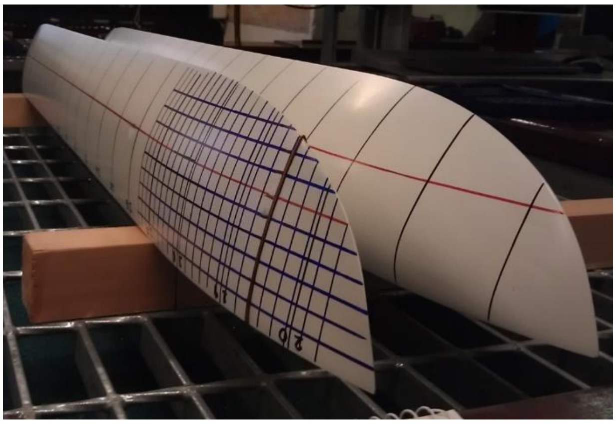

Figure 6. Photograph of model V2 showing the trip wire to initiate transition.

The coefficients defined herewith are all located in the horizontal plane, normal to gravity. Drag (F_D) is the force in the direction parallel with the onset flow, so in the tank it is the force along the tank axis, and the drag coefficient is

$$C_D = \frac{F_D}{\frac{1}{2}\rho A V^2}. \tag{2}$$

Lift (F_L) is the force in a direction normal to the onset flow, so in the tank this is the force perpendicular to the tank axis. The lift coefficient is

$$C_L = \frac{F_L}{\frac{1}{2}\rho A V^2}. \tag{3}$$

The resistance coefficient is defined here as the force along the longitudinal axis of the model. When there is no leeway it is the same as the drag coefficient. When the model is at a leeway angle λ, also here referred to as the yaw angle, the resistance coefficient is

$$C_R = C_D \cos\lambda - C_L \sin\lambda\,. \tag{4}$$

The side force is normal to the resistance, and the side force coefficient is

$$C_S = C_D \sin\lambda + C_L \cos\lambda\,. \tag{5}$$

2.6 Prediction of Drag and Side Force from the CFD Simulations

Boeck (2010) and Boeck et al (2012) modelled the three hull shapes which were the main subject of the investigation. Predictions of lift and drag were made at leeway angles of 0°, 5°, 10° and 15°, at a speed of 1.543 m/s (3 knots) which corresponds to a Froude number of 0.12. He validated his methodology by modelling the so-called Wigley hull, which has been well studied and for which there are numerous experimental data available (for instance, Hayashi, 1988; Maruo, 1990; Kracht 2007). For example, comparisons in Boeck (2010) with experimental data from Wong (1994) show that resistance coefficient differences for Froude numbers of 0.225 and 0.267 are less than 4% and for a large Froude number of 0.316 the CFD under-predicts the experimental value by 12%.

The results available in Boeck (2010) use the wetted surface area of the hull as the reference area, which is different for all the three models. In order to eliminate this variable, it was decided that for the present work the reference area would always be the immersed projected side area, which is significantly smaller than the wetted area, and would therefore lead to higher force coefficients. The values of the various areas for the models are given in Table 2. The results of the present study are compared with those of Boeck (2010) in Section 3.2, where the coefficients have been recomputed using the immersed projected side area for consistency with the rest of the paper.

2.7 Fixed Sink and Trim tests

Tests were conducted with “fixed sink and trim.” This means that the heave post is locked so that the model cannot move vertically, nor pitch. Such tests are simpler to conduct than “free to sink and trim” tests, as the former do not require the pitching moment to be calculated for a given towing force. Since the primary objective of the test programme was to understand how the hull shape affected the lift or side force when the model had various amounts of leeway, a test schedule was prepared which was a matrix of speeds ranging from 0.4 m/s to 1.6 m/s, and leeway angles from 0° to 24°. As the test progressed, there were changes based on observations of tests, such as the speed and leeway which caused water to spill onto the deck. The actual tests that were undertaken are shown in Table 3. Note in Table 3 that U corresponds to the rounded hull, V1 to the wide Vee hull, and V2 to the narrow Vee hull. Although yaw angle setting holes were pre-drilled at 2° intervals, preliminary testing revealed that such a small angle change was not needed, and so the tests were done at 4° intervals.

Normal tank testing procedures were used to carried out the tests, such as waiting for sufficient time for the water to settle between runs, checking the waterline height each day after skimming, zeroing the load cells, repeating the same test from the last run of the previous day to the first run of the following day, and repeating runs where the results looked questionable.

Table 3. Tests done for different values of λ and V from 2 July – 5 July 2013 in the Newcastle Towing tank on slender hulls.

	0.4 m/s			0.8 m/s			1.0 m/s	1.2 m/s			1.6 m/s	
0°	U	V1	V2	U	V1	V2		U	V1	V2	U	V1
4°	U		V2	U		V2		U		V2	U	
8°	U	V1	V2	U	V1	V2		U	V1	V2		V1
12°			V2			V2				V2		
16°	U	V1	V2	U	V1	V2		U	V1	V2		V1
24°	U	V1		U	V1		V1	U	V1			

3. RESULTS

3.1 Drag, Lift, Resistance and Side Force as a Function of Speed

Here the force results are plotted against model speed. The test speeds were nominally 0.4 m/s, 0.8 m/s, 1.2 m/s and 1.6 m/s. These correspond to Froude numbers of 0.12, 0.23, 0.35 and 0.47. Drag is plotted against speed in Figure 7 for all three models. Several features are apparent in the figure. The narrowest model, V2 has the lowest drag for a given speed, followed by the wider Vee model (V1) and the rounded model (U). The displacements of the test models U, V1 and V2 are 3.8 kg, 2.1 kg, and 1.3 kg, respectively, and they were tested at the same draught. Therefore we expect that the reduction in displacement of the models as they become narrower will also contribute to a reduction in drag.

The drag increases as speed increases, as expected, and the drag increases as the leeway angle is increased, although the V1 and V2 models have very similar drag when yawed at 16°. Drag coefficient is plotted against speed in Figure 8. Here it is evident that the coefficients are essentially constant over the speed range of the tests. It is more evident that yawing the model to produce leeway gives a significant increase in the drag coefficient as expected. The V2 model was not tested at a leeway angle of 24°. Note that the reference area here and subsequently is the projected immersed side area, which is the same for the three models.

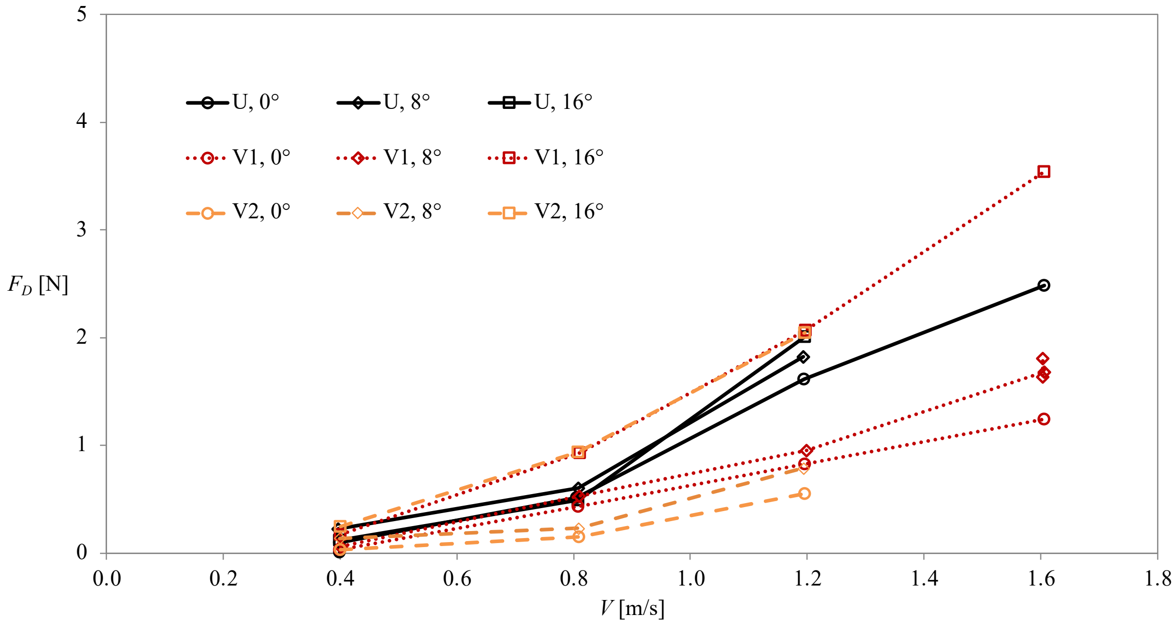

Figure 7. Fixed sink & trim, drag versus speed for all three models.

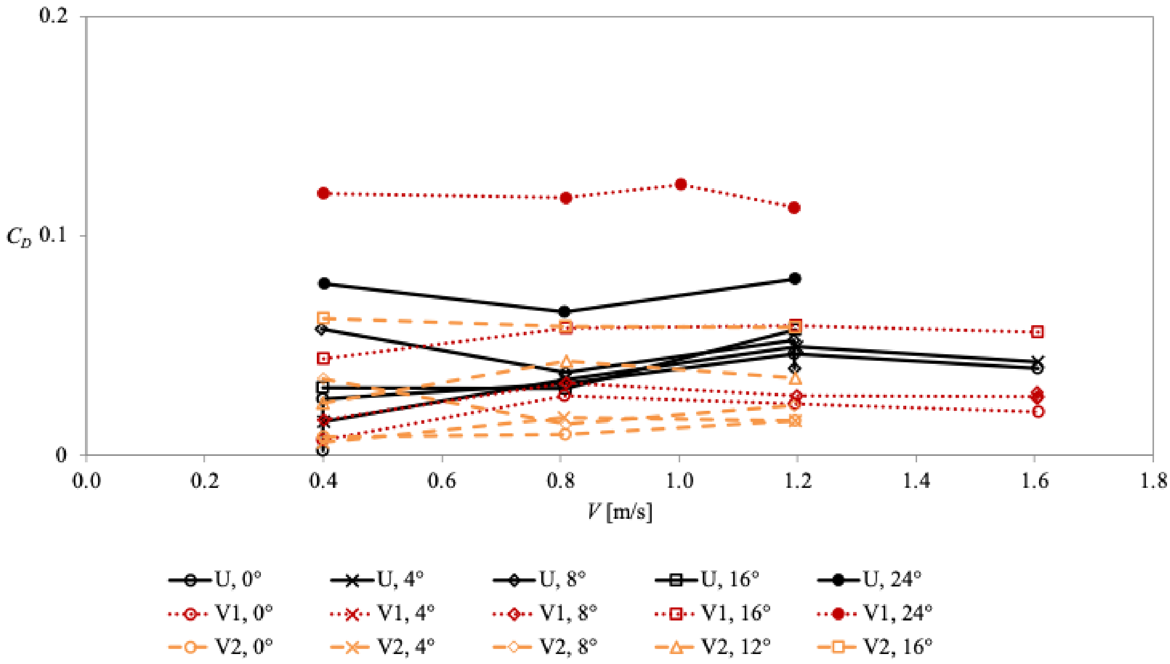

Figure 8. Fixed sink & trim, drag coefficient versus speed for all three models.

Resistance coefficient is plotted against speed in Figure 9. One might expect the resistance and drag coefficient plots to look similar, and indeed this is the case for the low leeway angles, but for larger angles the significant amount of lift that is generated (of order twice the drag) has a component that subtracts from the resistance, which lowers it significantly. This also has the effect of reordering the results. The rounded U model (black solid lines), which is not so good at generating lift, has the highest resistance, and conversely the narrow V2 model (yellow dashed lines) has the lowest resistance coefficient.

The lift and side-force coefficients are the primary foci of this work, and lift is plotted against speed in Figure 10. It can be seen that the lift is approximately twice the drag, and that as the models become narrower, they become more efficient at generating lift. The U model at 0° shows a small negative lift at a speed of 1.6 m/s. This is due to experimental error; possibly a very small angle misalignment of the model.

The lift coefficients are shown in Figure 11, and as observed for the drag coefficients, the lift coefficients are also relatively unaffected by the speed over the range tested, although there is perhaps a slight trend to smaller coefficients as speed is increased. It is also evident that there is a much larger increase in lift coefficient between the rounded model U and the wide Vee model V1, with a smaller difference to the V2 model.

The side force coefficient is plotted against speed in Figure 12. It can be seen that this figure is similar to Figure 11. The results are ordered the same, and the main difference is that the side force coefficient is a little larger than the lift coefficient for the larger leeway angles, as the drag has a component which adds to the side force. The side force coefficients are also relatively unaffected by test speed. In both Figures 11 and 12, the ranking of lift and side-force from the three lines can be seen by studying the lines with the open square symbols (16° leeway). Similar to the CFD results, these experimental results show that having a narrower hull enables more lift and side-force to be generated for a given leeway angle.

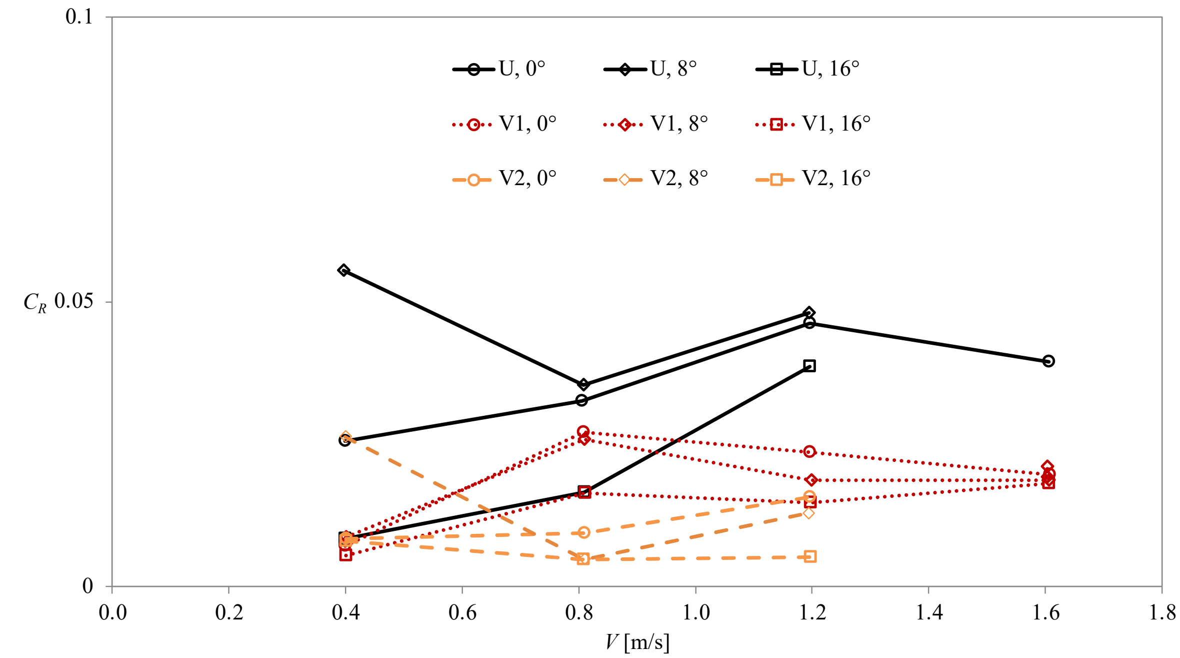

Figure 9. Fixed sink & trim, resistance coefficient versus speed for all three models.

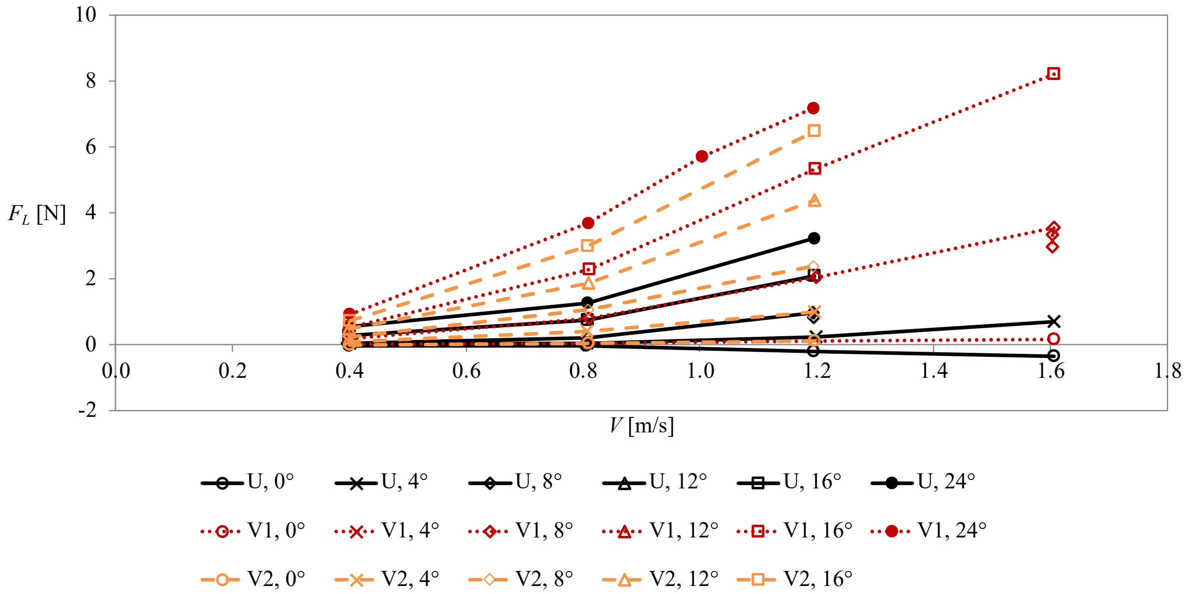

Figure 10. Fixed sink & trim, lift versus speed for all three models.

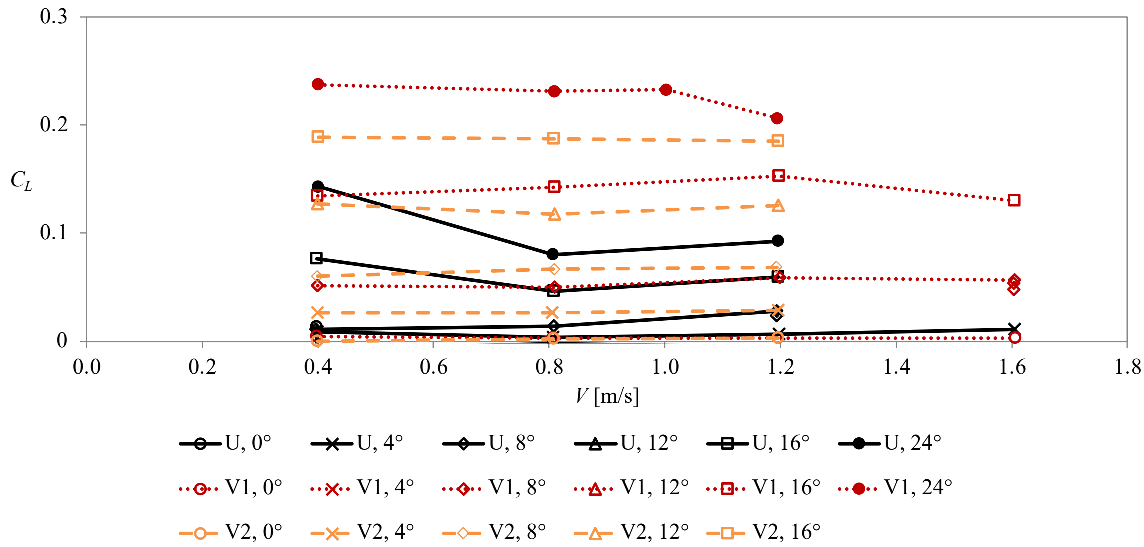

Figure 11. Fixed sink & trim, lift coefficient versus speed for all three models.

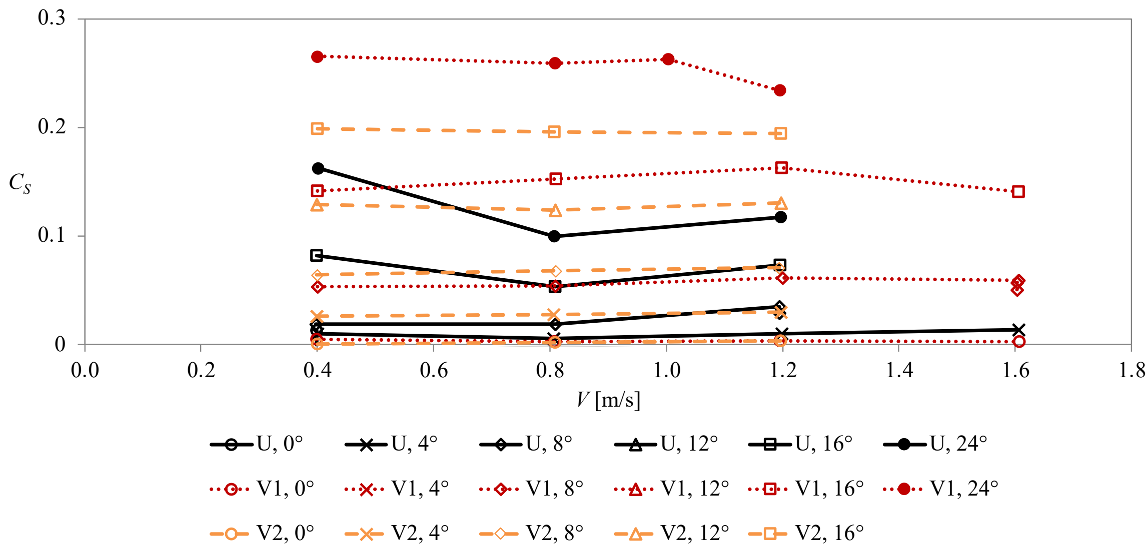

Figure 12. Fixed sink & trim, side force coefficient versus speed for all three models.

3.2 Drag, Lift, Resistance and Side Force as a Function of Leeway Angle

Since one of the objectives of carrying out this work was to obtain better estimates of side force for Polynesian sailing vessels as a function of leeway angle, the results are also shown in that manner. This presentation also enables them to be compared with the CFD predictions available in Boeck (2010), which were carried out at a speed of 3 knots (1.5433 m/s) for several leeway angles.

Drag is plotted against yaw in Figure 13 for all three models. Here it can be seen that drag increases with increasing yaw angle for all three models, and that the rounded U model has the highest drag for a given yaw, followed by the moderate V1 model and by the narrowest V2 model. The drag coefficient is plotted against leeway angle in Figure 14. Although the variation in the results indicates some effect of experimental error, it is clearly evident that the three models show different trends. The drag coefficient for the rounded U model does not increase as quickly with yaw angle as does the drag coefficient for the V1 model, and the narrowest V2 model shows the most rapid increase in drag coefficient with yaw angle. Hence at a yaw angle of 0°, the drag coefficient is highest for the U model and lowest for the V2 model, but at a yaw angle of 16° the order is reversed. The V2 model was not tested at a yaw angle of 24°, which perhaps is unfortunate, as it might have shown up this effect even more clearly. All models had the same drag coefficient at an angle of about 7°.

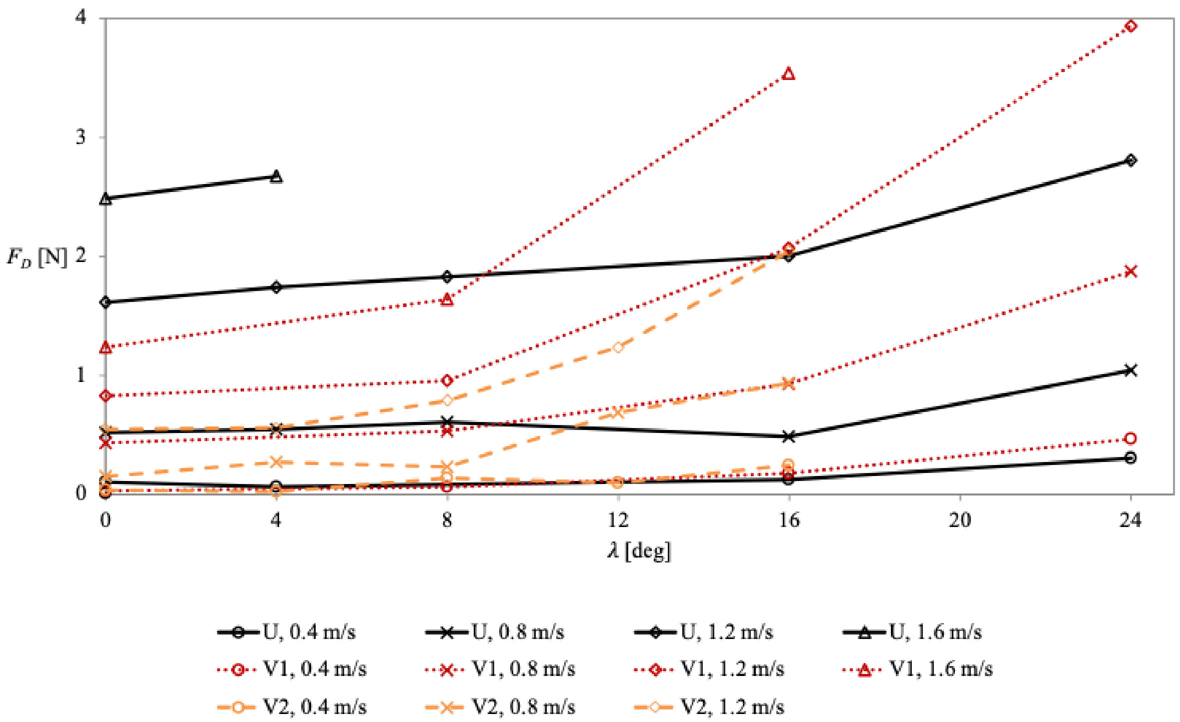

Figure 13. Fixed sink & trim, drag versus leeway angle for all three models.

Figure 14 also shows the CFD predictions for drag coefficient as lines without symbols. Boeck (2010) and Boeck et al (2012) used CFD to predict the drag of a full-scale vessel at a speed of 1.543 m/s, and for coarse increments of leeway angles of 0°, 5°, 10° and 15°, for all the three hull shapes. Boeck's data were fitted by second order polynomial functions and used to plot the lines shown. Note that there is a disparity in the CFD and tank Reynolds numbers, and this point is returned to later when the tank coefficients are scaled to full-scale Re using the Prohaska-Hughes method. It can be seen that the CFD predictions are low for the rounded U model, but the trend of increase with yaw angle is represented in a similar fashion both in the CFD and model tests. Interestingly, the Froude number corresponding to a model test speed of 0.4 m/s is 0.12, which converts to a speed of 1.26 m/s at full-scale.

The resistance coefficient is plotted against leeway angle in Figure 15. There is a rather striking difference between the drag and resistance coefficient plots, which may seem rather surprising. The resistance coefficients are generally lower than the drag coefficients, for the same reason as discussed in the previous section (Section 3.1), that the lift subtracts from the resistance, particularly at the higher leeway angles, where it can be seen in Figure 15 that the coefficients actually decrease with increasing yaw angle. The second major difference with the drag coefficient plots is that the resistance coefficient is always highest for the rounded U hull, and lowest for the narrow V2 hull, across the entire yaw angle range.

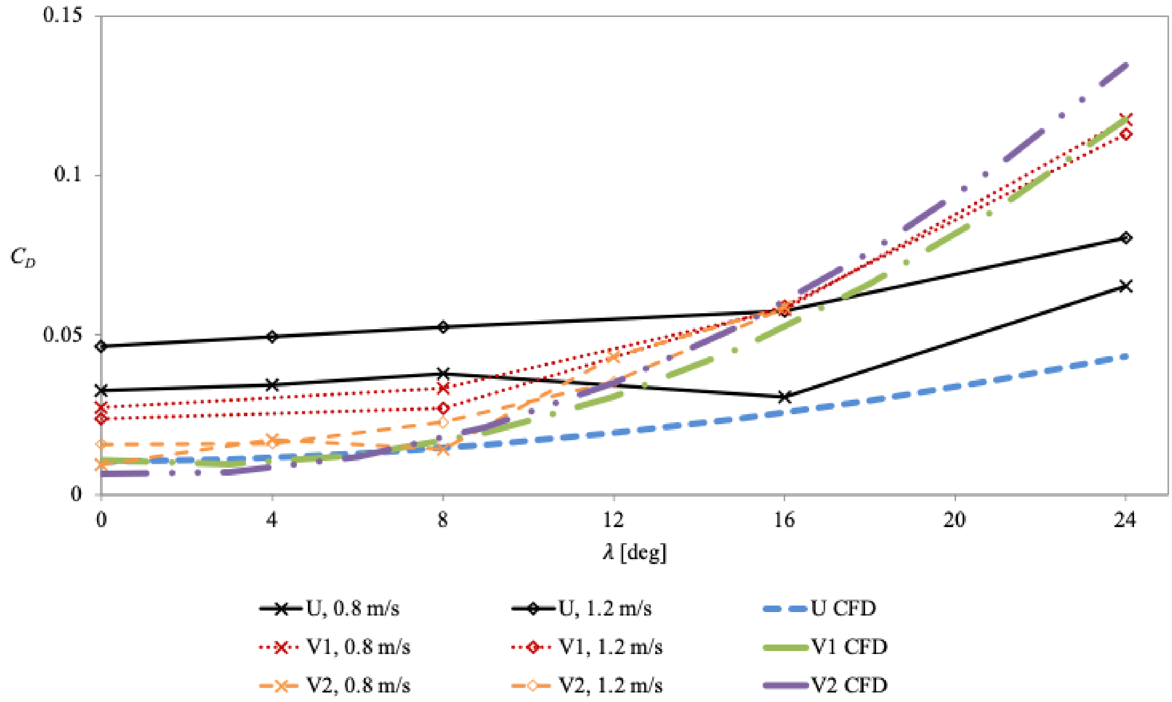

Figure 14. Fixed sink & trim, drag coefficient versus leeway angle for all three models, and comparison with CFD predictions (Boeck, 2010 and 2012).

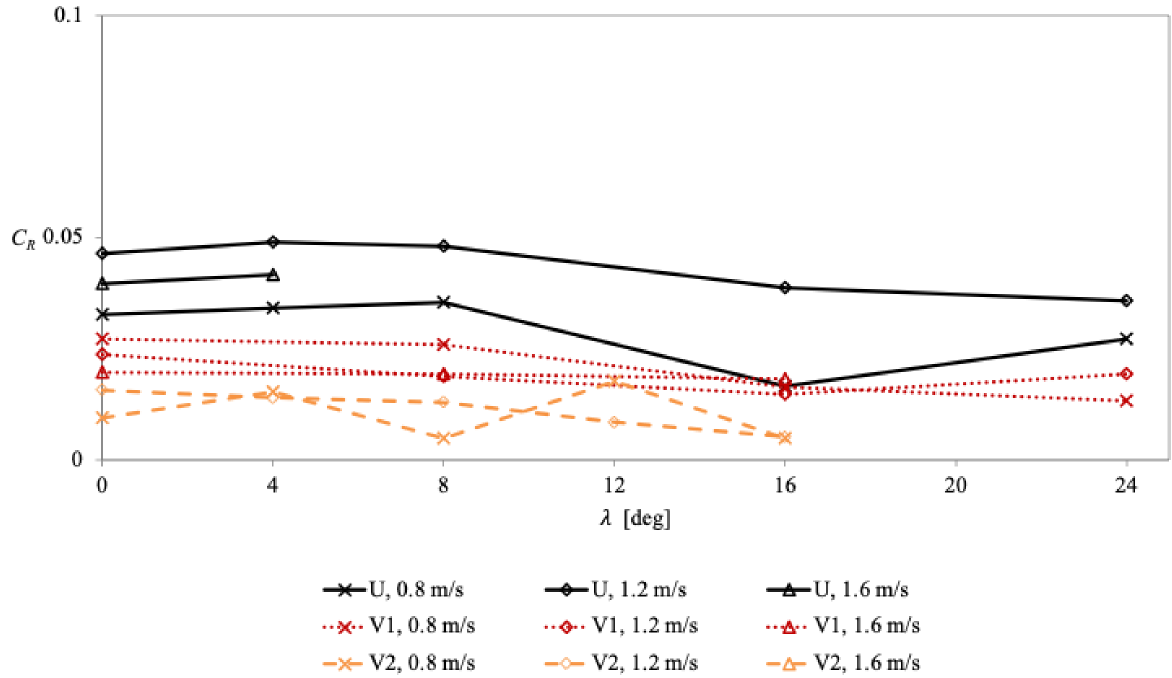

Figure 15. Fixed sink & trim, resistance coefficient versus leeway angle for all three models.

The lift is plotted against leeway angle in Figure 16 for all three models. It is evident that lift increases with increasing yaw angle, and that the narrowest V2 model is the best at producing lift, and the rounded U model is the worst at producing lift. Turning lift into a coefficient, as shown in Figure 17, puts the lines into clear groups, with it even more evident how a rounded hull is much worse at producing lift compared to having a narrow Vee. The effect of model speed can be seen to have a relatively minor effect on the coefficients for the V1 and narrow V2 model, but a slightly larger effect on the rounded U model.

The CFD predictions of the lift coefficient from the work of Boeck (2010) and Boeck et al (2012) are also plotted in Figure 17. Boeck carried out simulations on full-scale vessels of identical shape to the present tank test models, at a speed of 3 knots (1.5433 m/s), for a range of yaw angles. His data have been fitted to second order polynomials and plotted as shown. It is clearly evident that the agreement is extremely good, and that the CFD predictions lie within the band of experimental results for each of the three models, up to a leeway angle of 16°, and beyond that angle, the predictions are still rather good.

The side force coefficients are plotted in Figure 18. These can be seen to look almost identical to the lift coefficients in Figure 17. There are groups of lines bunched together for each of the test models showing that the coefficients are only weakly dependent on speed.

It should be noted at this point that the CFD simulations were carried out at full-scale, i.e. at a Reynolds number of about 20 million, whereas the present tank results were carried out at a Reynolds number range between 5×10^5 to 2×10^6, or more than one order of magnitude less. Whereas there are well developed procedures for scaling tank resistance results to full-scale Reynolds numbers, it is not clear that there are similar procedures for scaling the lift or side force results. Hence the comparisons shown in Figures 14 and 17 are for different CFD and tank model Reynolds numbers. No Reynolds number scaling corrections have been applied to the lift and side force results presented in the paper, while the effect of Reynolds number on the drag is discussed in the next section.

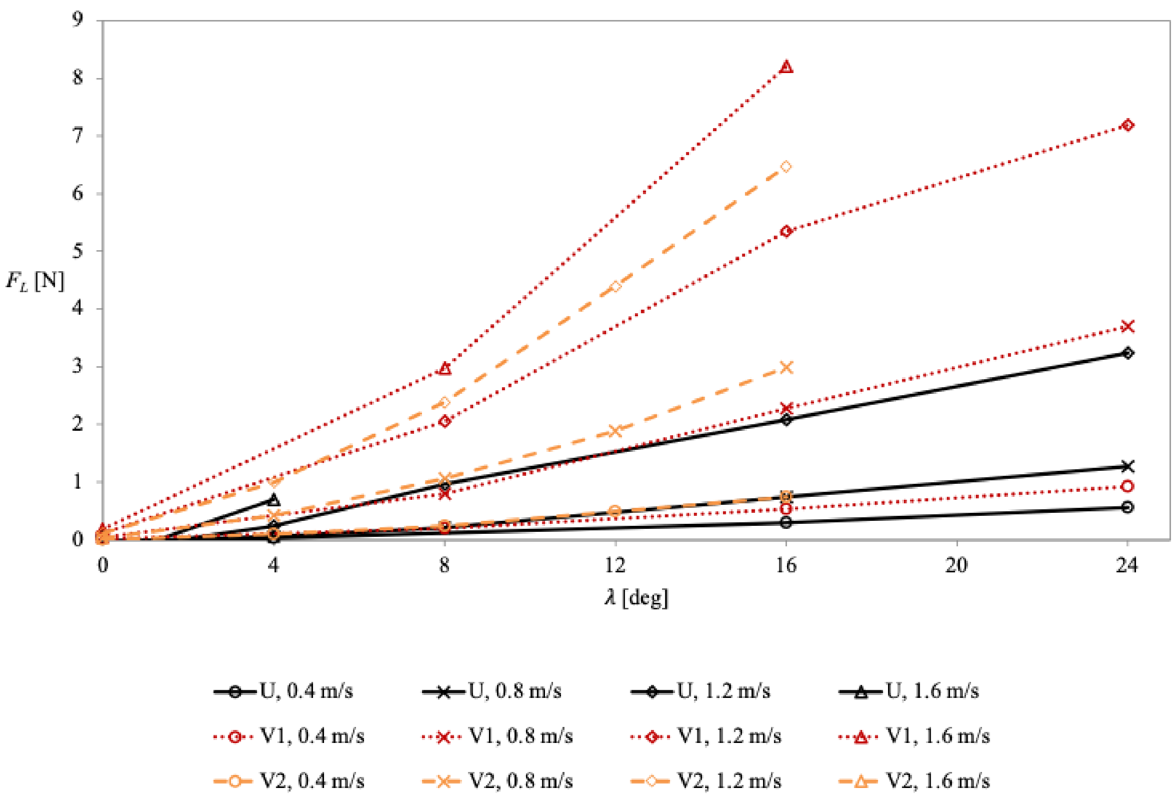

Figure 16. Fixed sink & trim, lift versus leeway angle for all three models.

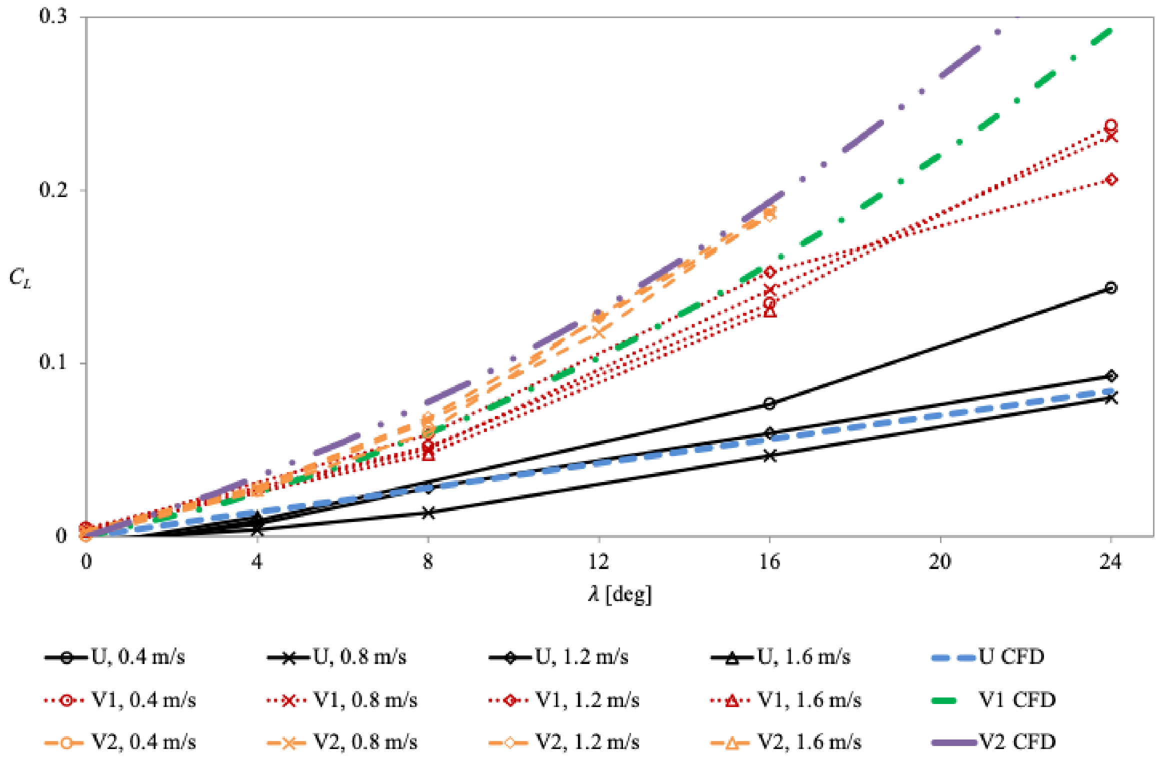

Figure 17. Fixed sink & trim, lift coefficient versus leeway angle for all three models, and comparison with CFD predictions (Boeck, 2010 and 2012).

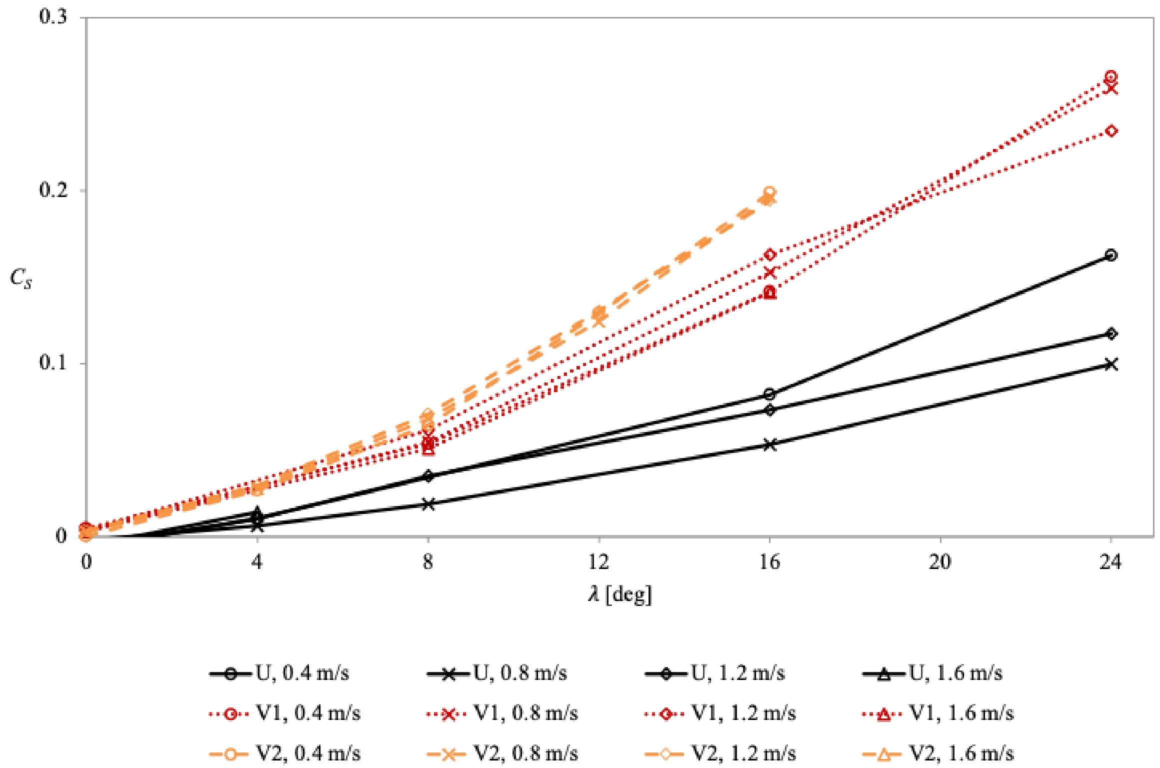

Figure 18. Fixed sink & trim, side force coefficient versus leeway angle for all three models.

4. DISCUSSION

The agreement between experimental and numerical results using the simulations of Boeck (2010) and Boeck et al (2012) allows some insights on the flow and pressure fields to be gained, and thus on the underlying mechanisms of the observed force differences between the three hull shapes. Boeck (2010) undertook numerical simulations of the three hulls sailing at 3 knots with a 10° yaw angle. They solved the steady incompressible Navier-Stokes equations for Newtonian fluids for both air and water with a finite volume solver (Ansys CFX), a volume of fluid approach for the free surface, and a shear stress transport turbulence model. Verification and validation were undertaken for a mesh of approximately 1.7×10^6 cells (made with Ansys ICEM CFD) with towing tank tests on a Wigley hull model.

Figure 23 shows the flow velocity vectors projected onto a cross-sectional plane at midships, as well as the surface pressure distribution (p) on the forward hull surface. The velocity is made non-dimensional by dividing by the ship velocity ($V =$ 3 knots), while the pressure is the difference between the static pressure and the hydrostatic pressure. The yaw angle is such that the flow velocity with respect to a hull-fixed frame flows from right to left in the figure.

The in-plane velocity v accelerates around the bottom of the hull, which is the maximum width of the obstacle observed by the free stream flow. Past this point, in the case of the rounded U-hull (Figure 23a), the flow follows the shape of the hull because of the Coanda effect and a thick, yet attached, boundary layer is observed. Conversely, on the V1 and V2 hulls (Figures 23b and 23c), because of the sharp edge at the bottom of the hull, a shear layer separates and rolls up into a coherent vortex. It is noted that these are the solutions of steady-state simulations, thus the instantaneous coherence of this vortex cannot be assessed. In the time-averaged sense, however, the vortex is associated with a low-pressure region on the downstream hull side (left in Figures 23b and 23c). The vortex is shown on the cross-section at midship, while the vortex footprint on the surface pressure clearly shows that the vortex develops at the bow and persists at least up to midship. The close pressure isolines also reveal that the effect of the vortex on the pressure is stronger near the bow that at midship. The increasing difference between the pressure on the two sides of the hull from hull U to V2, accounts for the increasing side force shown in Figure 18.

To further support the hypothesis that the increased side force and reduced resistance is what drove the Pacific vessels' evolution from rounded to Vee-shaped, Boeck (2010) used the computed hydrodynamic forces as input for a Velocity Prediction program (VPP). A VPP solves numerically Euler's equations for the vessel, where the aerodynamic and hydrodynamic forces are described as a function of the wind and vessel velocities. The aerodynamic forces were taken from Marchaj (1966) for a rig similar to that used on Pacific canoes. In this two-degrees-of-freedom VPP, for a specified true wind speed and direction (i.e. with respect to a earth-fixed observer), the vessel velocity and yaw angle satisfying Euler's equations are computed. Figures 23d- 23f show the results of the VPP for the hulls U, V1 and V2, respectively. For each tested wind velocity from 3 m/s to 6 m/s, the U-shaped hull cannot sail closer than 70° to the true wind at more than 1 m/s. However, the narrowest V1 and V2 hulls can sail at a true wind angle of around 60° at significant speeds, and the vessels' speeds increase with increasing wind speed. Overall, these numerical results, now supported by the present experimental data, are consistent with the hypothesis that technological advances in canoe design were adaptive and canoes of different hull shape were used for different purposes: V-shaped canoes had higher lift and lower resistance for upwind voyaging; U-shaped canoes had less drag when sailing downwind. Note, however, that the VPP results are for vessels with the same draught, so the displacements reduce from U to V1 to V2 hulls, and this reduction in displacement, as well as the hull shape change, have both contributed to the VPP performance results. Both kinds of canoe developed optimal performance for their function, with U-shaped hulls better for load carrying downwind, and V-shaped canoes better for upwind exploratory voyaging.

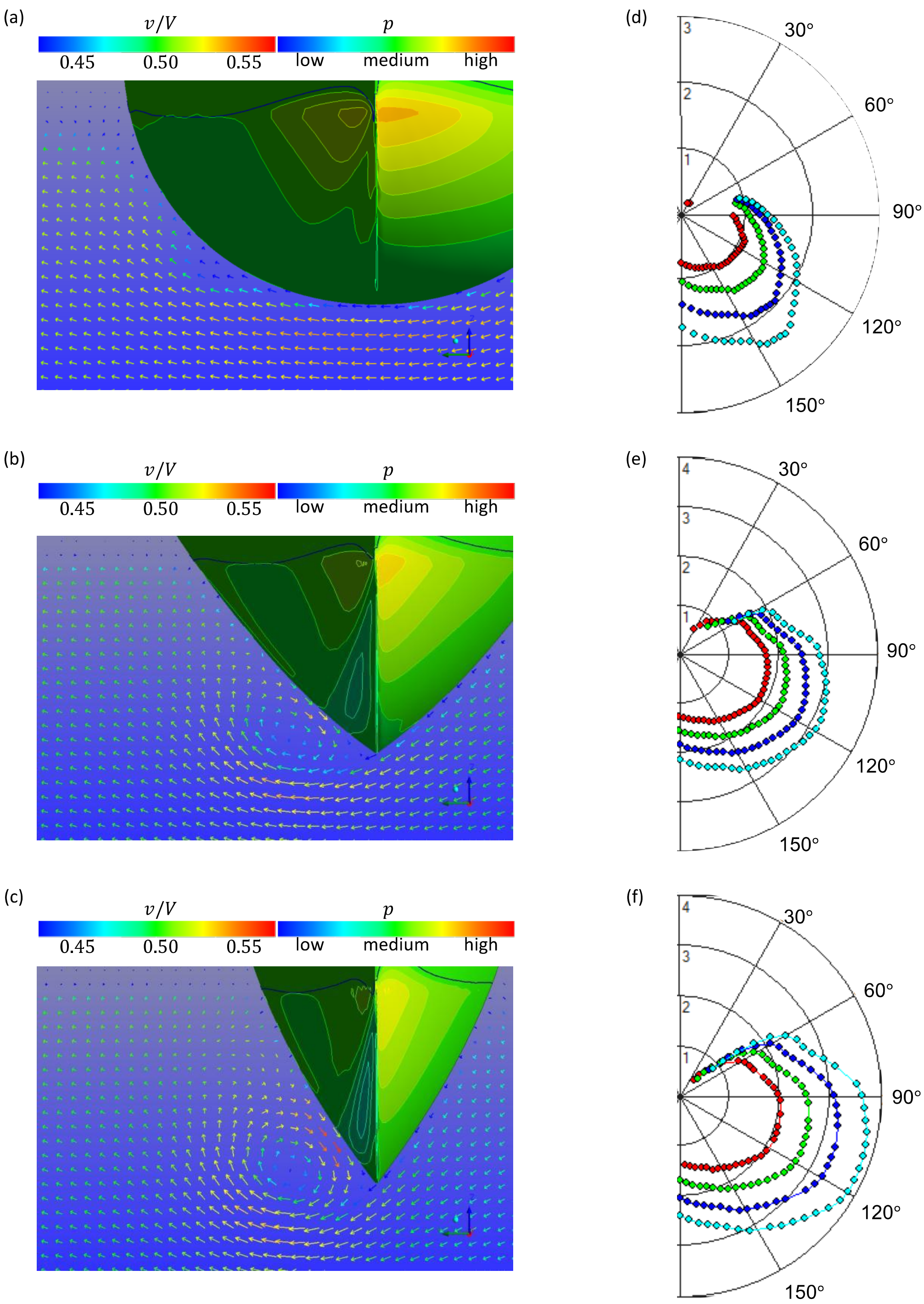

Figure 19. Velocity vector field on the cross-sectional plane at midships, and pressure coefficient distribution on the forward part of the hull surface computed with CFD for U (a), V1 (b) and V2 (c) sailing at 3 knots; and polar plot result of the VPP for U (d), V1 (e) and V2 (f) for a wind speed of 3 m/s (red), 4 m/s (green), 5 m/s (blue), and 6 m/s (turquoise). The polar coordinate shows true wind angle, and the radial coordinate shows the vessel speed. All plots edited from Boeck (2010).

5. CONCLUSIONS

The three simplified 1:10-scale models of ancient Pacific multi-hull vessels are investigated to explore whether the shift from rounded to Vee-shaped hulls over the centuries could have been driven by the need to generate sideforce and sail upwind. Three models with the same waterline length, draft, and projected side area were manufactured and tested in the Towing Tank at Newcastle University with fixed sink and trim. The model-scale results show that the most rounded hull, representative of the first Pacific vessels made directly from trees, has the minimum drag at high yaw angles. In contrast, the narrowest hull shows the minimum drag at low yaw angles, but also the maximum lift and side force. Furthermore, because the lift has a negative component on the resistance (aligned with the longitudinal axis of the hull), the narrowest hull also shows the minimum resistance.

Tests were performed at a Reynolds number ranging between 4×10^5 and 1.7×10^6, and a Froude number from 0.12 and 0.48. These results should not be extrapolated for higher Froude number values. The drag coefficients were corrected from the tank Reynolds number value to the full-scale value, which is about 2×10^6, using the Prohaska method. The form factor decreases with the slenderness of the hull, and thus also with the block coefficient. It was found that the correction resulted in a reduction of drag coefficient of the order of 0.01. This value is relatively small, and is probably of the same order, or in fact smaller, than the experimental error.

It was found that there was good agreement between the side-force predicted numerically by a previous author and experimentally determined values from tank test results on the three different models. The numerical predictions that narrower Vee-shaped hulls would generate more side-force when at leeway than a rounded hull was confirmed by the present tank test results.

These results are consistent with the hypothesis that Pacific vessels evolved from U-shaped to V-shaped with the increased need to sail upwind. They did so to explore greater areas of the Pacific Ocean from the point of origin, and V-shaped vessels became most developed in Micronesia. The metadata underpinning the results, including the iges files of the geometries, are available through the University of Edinburgh DataShare repository (Flay et al, 2022).

ACKNOWLEDGEMENTS

This research was carried out as part of the Sailing Fluids project funded jointly by the EU and by NZ. The grant details are as follows. EU - Call: FP7-PEOPLE-2012-IRSES. Funding scheme: MC-IRSES (International Research Staff Exchange Scheme (IRSES)). Proposal number: 318924. Proposal acronym: SailingFluids. NZ - IRSES Application 2012-318920-SAILING FLUIDS funded by the Royal Society of New Zealand. The first author was assisted in carrying out the towing tank tests by Alexander Blakeley, Joshua Taylor, and Nick Velychko whose contributions are gratefully acknowledged. The support provided by the Newcastle University technical staff in the laboratory is also gratefully acknowledged.

AUTHOR CONTRIBUTIONS

RGJF and GJI conceived the original CFD study by Boeck (2010) and Boeck et al. (2012), and RGJF conceived and undertook the present experimental study. GJI and IMV contributed to the design of the study and presentation of the results. RGJF wrote the first draft of this manuscript, which was edited and approved by all authors.

APPENDIX: UNCERTAINTY ANALYSIS

The total uncertainty is estimated as the sum of the squares of the bias limit B and the precision P, assuming that they are independent to each other, as

$$U = \sqrt{B^2 + P^2}. \tag{A1}$$

The total bias limit is the contribution to the uncertainty of the errors that do not vary across the set of conducted experiments. The total bias for a coefficient C of a generic force F is

$$B = \left[\left(\frac{\partial C}{\partial \lambda} B_\lambda\right)^2 + \left(\frac{\partial C}{\partial \rho} B_\rho\right)^2 + \left(\frac{\partial C}{\partial A} B_A\right)^2 + \left(\frac{\partial C}{\partial V} B_V\right)^2 + \left(\frac{\partial C}{\partial F} B_F\right)^2\right]^{\frac{1}{2}}, \tag{A2}$$

where B_λ, B_ρ, B_A, B_V and B_F are the bias limits of the yaw, water density, immersed projected side area, carriage velocity and force, respectively. The variation of the force coefficient with lambda ($\partial C/\partial \lambda$) is computed conservatively from the derivative of the second order polynomial approximation of the lift coefficient of V1 at 0.4 m/s (Figure 17): $C_L = 0.0002\lambda^2 + 0.0045\lambda + 0.0039$. The maximum yaw bias limit (B_λ) is estimated in $0.5°$. The remaining partial derivatives in equation A2 are computed from the definitions of coefficients in equations 2 and 3, yielding to

$$B = \left[\left((0.0004\lambda + 0.0045)B_\lambda\right)^2 + \left(\frac{-2F}{\rho^2 V^2 A} B_\rho\right)^2 + \left(\frac{-2F}{\rho V^2 A^2} B_A\right)^2 + \left(\frac{-4F}{\rho V^4 A} B_V\right)^2 + \left(\frac{2}{\rho V^2 A} B_F\right)^2\right]^{\frac{1}{2}}, \tag{A3}$$

The density bias limit (B_ρ) is estimated from the density variation with the water temperature T,

$$B_\rho = \left|\frac{\partial \rho}{\partial T}\right| B_T, \tag{A4}$$

where B_T is the bias limit of the water temperature, and the sensitivity of the density with temperature ($\partial \rho/\partial T$) is the derivative of equation 1. During the tests, the water temperature was estimated between a minimum $T_m = 14°$ and a maximum $T_M = 15°$. Therefore, $B_T = T_M - T_m = 1°$.

The area bias limit is conservatively estimated in $1\%A = 0.000488$ m^2, the velocity bias limit is conservatively estimated in 0.03 m/s, and the force bias limit in 0.06 N. By substituting these values in equation A3, one finds that the bias limit is dominated by the force bias, and it increases with decreasing speed. Specifically, the bias limit is lower than 0.01 for any flow velocity but 0.4 m/s, where it is as high as 0.2.

The precision P is estimated at 95% confidence level as

$$P = \frac{2\sigma}{\sqrt{n}}, \tag{A5}$$

where σ is the standard deviation of the force coefficient of the n sampled force values. The precision is estimated in 0.01, resulting in an overall uncertainty lower than 0.02 for any flow velocity greater than 0.4 m/s.

REFERENCES

Adler, A. (1990). Written discussion of Larsson, L., Kim, K.J. and Zhang, D.H. (1990). A Method for Resistance and Flow Prediction in Ship Design. *Society of Naval Architects and Marine Engineers Transactions,* vol. 98, no. 532

Boeck, F. (2010), Side Force Generation of Slender Hulls, *Study Thesis*, TU Berlin, Germany.

Boeck, F., Hochkirch, K., Hansen, H., Norris, S., Flay, R.G.J. (2012). Side Force Generation of Slender Hulls – Influencing Polynesian Canoe Performance, *4th High Performance Yacht Design Conference*, Auckland, New Zealand 12-13 March.

Dudley, L., Irwin, G., Flay, R. G. J., and Damon, F. (2021). Experimental Voyages by Real and Virtual Traditional Canoes of the Kula Area, Papua New Guinea, Provide Insights into Ancient Sailing Technology of the Pacific Ocean and for the Settlement of Polynesia. *Journal of Pacific Archaeology* vol. 12, pp. 32-45.

Flay, R. G. J., Irwin G. J. and Viola I. M. (2022). Hydrodynamics of Three Slender Models Resembling Pacific Canoe Hulls, 2012-2022 [dataset]. University of Edinburgh. https://doi.org/10.7488/ds/3785.

Flay, R. G. J., Norris, S., Halliburton, K. A., Jowett, D. A., and Erriu, N. (2008). Performance Prediction of the Olympic Variant Tornado Class Catamaran. *3rd High Performance Yacht Design Conference*, Auckland, New Zealand 1-4 December.

Flay, R. G. J., Viola, I. M., and Irwin, G. J. (2019). Hydrodynamics of Three Slender Models Resembling Polynesian Canoe Hulls. *The 23rd Chesapeake Sailing Yacht Symposium*. US Naval Academy, Annapolis, MD, USA, 15-16 March.

Finney, B., (2006). In K.R. Howe (ed.) *Waka Moana: Voyages of the ancestors.* Auckland: Bateman Press, pp. 100-153.

Froude W. (1955), *Observations and Suggestions of Determining by Experiments the Resistance of Ships,* Correspondence with Admiralty, 1868, Reprinted in *The Papers of William Froude*, RINA, 1955

Haddon A.C., and J. Hornell (1997). *Canoes of Oceania*. Honolulu: Bishop Museum Press.

Hayashi, Y. K. (1988). *Measurement of Wave Pattern Around a Yawed Ship Model.* Yokohama National University, Japan: Graduation thesis.

Hoerner, S., and Borst, H. V. (1985). Chapter XVII: Characteristics of Small Aspect Ratio Wings. In *Fluid Dynamic Lift* (Second Edition). Mrs. Liselotte A. Hoerner.

Hughes G. (1954). *Friction and Form Resistance in Turbulent Flow, and a Proposed Formulation for use in Model and Ship Correlation,* Transactions of RINA, vol. 96.

Hunter W.S. and Joubert P.N. (1988). Side Forces on a Ship's Hull, *Journal of Ship Research*, vol. 32, no. 3, pp. 203-207.

Irwin, G. (1992). *The Prehistoric Exploration and Colonisation of the Pacific*. Cambridge: Cambridge University Press.

Irwin, G., and Flay R. G. J. (2015). Pacific Colonisation and Canoe Performance: Experiments in the Science of Sailing. *Journal of the Polynesian Society,* vol. 124, pp. 419–443.

Irwin, G., D. Johns, R.G.J. Flay, F. Munaro, Y. Sung and T. Mackrell. (2017). A Review of

Archaeological Maori Canoes (*waka*) Reveals Changes in Sailing Technology and Maritime Communications in Aotearoa /New Zealand, AD 1300-1800. *Journal of Pacific Archaeology*, vol. 8, pp. 31-43.

Irwin, G., Flay, R.G.J., Dudley, L., Johns, D. (2023). The Sailing Performance of Ancient Polynesian Canoes and the Early Settlement of East Polynesia, *Archaeology in Oceania*. DOI: 10.1002/arco.5277.

Irwin, G., Flay, R.G.J., Dudley, L., Johns, D. (2024). The Sailing Performance of Ancient Polynesian Canoes: Technological Innovations and Maritime Migrations", *The Oxford Handbook of Island and Coastal Archaeology*.

ITTC – Recommended Procedures and Guidelines 7.5-01-01-01 (2002). Model Manufacture, Ship Models. Revision 01.

ITTC – Recommended Procedures and Guidelines 7.5-02-01-03 (1999). Fresh Water and Seawater Properties. Revision 00.

Jackson, P.S. (1995). Performance Prediction for Olympic Kayaks. *Journal of Sports Sciences,* 1995, vol. 13, pp. 239-245

Jackson, P.S. and Bailey, K.I. (1996). Performance Prediction of a 'Flying Proa', *Waka Moana Symposium.* Ed.: Bader, Hans-Dieter and Peter McCurdy, New Zealand National Maritime Museum, 18 – 24 March, Hobson Wharf, Auckland, pp. 166-168, pp. 307-313.

Jacobs, B.A. (2003). Mathematical Modelling of Oceanic Canoe Performance, MA Thesis, Anthropology Department, The University of Auckland, NZ.

Johns, D., G. Irwin and Y.K. Sung (2014). An Early Sophisticated East Polynesian Voyaging Canoe Discovered on New Zealand's Coast. *Proceedings of the National Academy of Sciences,* vol. 111 no. 41, pp. 14728-14733.

Katz, J., and Plotkin, A. (2001). *Low Speed Aerodynamics*, 2nd Edn, Cambridge University Press, NY, USA.

Kracht, D.-I. A. (2007). *Skript Schiffshydrodynamik*. In D.-I. A. Kracht, *Kräfte am Schiff* (p. 23). Berlin: TU-Berlin.

Marchaj, C. A. (1996). *Sail Performance, Techniques to Maximize Sail Power,* Adlard Coles Nautical, London, UK.

Maruo H., S. W. (1990). Numerical Appraisal of the New Slender Ship Formulation in Steady Motion. *18th Symposium on Naval Hydrodynamics*, pp. 239-257.

Montenegro, A., R.T. Callaghan and S.M. Fitzpatrick (2014). From West to East: Environmental Influences on the Rate and Pathways of Polynesian Colonization. *The Holocene,* vol. 24, no. 2, pp. 242-256.

Thwaites, B. (1987) *Incompressible Aerodynamics* Dover Publications, UK.

van Oossanen, P. (1981). *Method for the Calculation of the Resistance and Side Force of Sailing Yachts. Calculator and Computer-Aided Design for Small Craft - The Way Ahead*, Royal Institution of Naval Architects.

Wong, H.L., (1994). Slender Ship Procedures that Include the Effects of Yaw, Vortex Shedding and Density Stratification, *Thesis*, University of British Columbia, Vancouver, Canada.